

NONCOHERENT 2D AND 3D SAR RECONSTRUCTION FROM WIDE-ANGLE MEASUREMENTS

Randolph L. Moses and Lee C. Potter

Department of Electrical and Computer Engineering
Ohio State University
2015 Neil Avenue, Columbus, OH 43210
moses@ece.osu.edu, potter@ece.osu.edu

ABSTRACT

This paper considers processing and visualization of radar scattering measurements from one or more wide-angle synthetic apertures. We consider both two-dimensional imaging and three-dimensional interferometric reconstructions.

A point-scattering assumption is poorly suited to wide-angle scattering; scattering objects within a target typically have narrow beam patterns, resulting in limited angles of persistence. We revisit traditional imaging in 2D or 3D to propose image formation techniques that use nonlinear, non-coherent combinations of subaperture data. The proposed techniques can be interpreted as approximations to a generalized likelihood ratio test.

For sufficiently high resolutions, individual reflectors are resolved, and hence the phase and amplitude of their responses are stable under small changes in viewing angle. This stability is in contrast to the scintillation observed in low-resolution data. Three processing techniques benefit as a result: interferometric measurement of 3D location is possible without wide-area averaging; polarimetric features may be used to describe local geometry; and, bandwidth enhancement is possible.

We illustrate processing and visualization techniques using X-band scattering predictions of a backhoe computed using X-patch. The reconstructions permit an approximation to the literal interpretation afforded by optical imaging, but with millimeter wave sensing. In addition, angle-dependent and polarization-dependent behaviors are displayed for enhanced recognition.

1. INTRODUCTION

We define a synthetic aperture radar (SAR) to be *wide-angle* if the aperture extent, $\Delta\phi$, exceeds the sector required for equal spatial bandwidth in range and cross-range

$$\Delta\phi > 2 \sin^{-1}(BW/(2f_c)) \quad (1)$$

This work was supported by the Air Force Research Laboratory under contract FA8650-04-1-1721.

where BW and f_c are the bandwidth and center frequency of the radar. For example, in an X-band system with $f_c = 9.5$ GHz and $BW = 1$ GHz, 15 cm resolution requires 5.7 degrees aperture. Wide-angle radar collections are motivated by both bi-static and multi-static radar systems that are capable of interrogating targets over wide angle spans. Improvements in inertial navigation and radar phase stability facilitate wide-angle coherent apertures; further, unmanned air vehicles (UAVs) operating as mono-static SAR systems or bi-static SAR receivers provide for wide-apertures with short data collection times. Wide-angle data collections are also possible in inverse SAR applications.

In this paper, we discuss three observations about wide-angle measurements and advocate data processing approaches motivated by these observations. First, wide-angle scattering deviates significantly from the point-scattering assumption; therefore, traditional coherent imaging and notions of resolution warrant re-evaluation for wide-angle SAR. Limited persistence of reflectors motivates our use of non-coherent combinations of subapertures for imaging in two and three dimensions; the imaging procedure may be interpreted as an approximation to a generalized likelihood ratio test.

Second, with sufficiently fine resolution cells, many individual reflectors become isolated. Without scintillation of unresolved reflectors, pixel amplitudes and phases are stable with respect to small changes in viewing angle. Consequently, three processing approaches are enabled: (a) interferometric processing may be used to estimate heights of individual reflectors; in contrast, successful use of IFSAR [1] has typically required spatial averaging and an assumption of locally flat terrain; (b) the stable phase allows polarimetric processing of individual reflectors, thereby revealing local target geometry; and, (c) the isolation of reflectors permits successful use of bandwidth extrapolation techniques.

Third, we illustrate by example that wide-angle interferometric apertures can provide three-dimensional target visualizations with near-literal interpretability. Results are computed from Xpatch simulations of X-band far-field scattering for a backhoe. The data collection does not require

Nyquist sampling in elevation. In addition, color may be used to encode angle and polarization dependence of the scattering.

2. WIDE-ANGLE IMAGE RESPONSES

Angle diversity improves spatial resolution for ideal point responses. For example, consider the 500 MHz bandwidth X-band cases illustrated in Figure 1 for four aperture widths. The phase history data support is shown on the left in f_x , f_y spatial frequencies; log magnitude images are displayed on the right. In each case, a polar-separable 35 dB Taylor window is applied for sidelobe reduction. Consider, for example, a 90 degree aperture: the maximum extents of sampling in the f_x and f_y frequencies are 3.2 GHz and 14.5 GHz, respectively. Consequently, the wide-angle aperture greatly enhances the resolution in both range and cross-range, as defined by the 6 dB image contour.

However, sidelobe levels are high and, by the Schwarz inequality (time-frequency uncertainty principle), are due to the area of support in the phase history, not the maximum extent. Moreover, the point spread function is less relevant for wide-angle imaging than for narrow-angle SAR because few, if any, reflectors have an angle-independent response across the full aperture. Previous studies [2, 3] show few reflectors persistent across even 10 to 20 degrees aspect. Effects limiting persistence, in addition to scintillation of neighboring reflectors, include blocking, self-occlusion, and physical extent of a radiating reflector. The effect of limited persistence is illustrated in Figure 2. Thus, for practical scattering behaviors, wide-angle apertures leave down-range resolution inversely proportional to bandwidth, as in narrow-band SAR. In Figure 2 we observe that image response is no longer characterized by a single impulse response shape. Further, coherent integration across an entire wide-angle aperture may obscure aspect-dependent behavior; and, integration beyond the persistence width does not improve signal-to-clutter ratio for imaged reflectors.

3. GLRT 2D IMAGING

The angle-dependent responses illustrated in Figure 2 motivate an imaging approach that departs from traditional approaches based on a point-scattering, or narrow-angle, assumption. A point response is independent of frequency and angle, with phase that encodes the location. Indeed, a traditional SAR image $I(x, y)$ may be viewed as the matched filter output for an isotropic point reflector that projects to point (x, y) in the imaging plane [4].

Instead, we propose generalized likelihood ratio test imager, whereby the image is the output for a filter matched to a limited-persistence reflector at (projected) location (x, y)

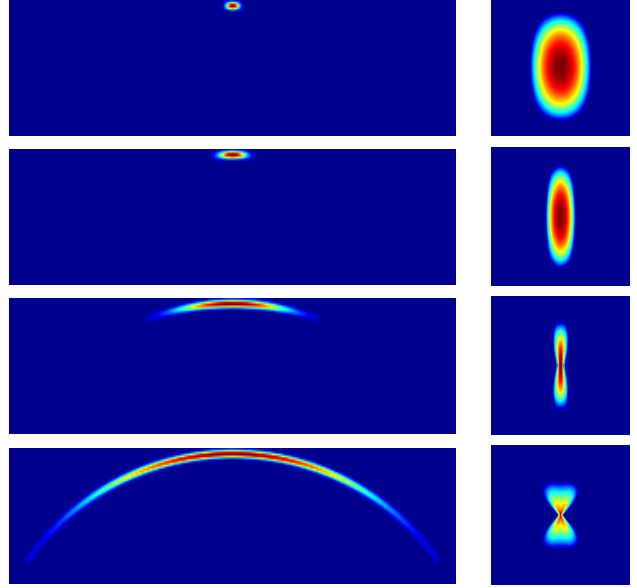


Figure 1: Windowed phase history data (left) and magnitude images (right) for an ideal point reflector. For each of four aperture widths (5, 10, 40, 110 degrees), the radar bandwidth is 500 MHz and center frequency is 9.5 GHz. The frequency support region is 5.4×18.0 GHz, and the images are 2×2 meters. The images are in logarithmic scale and show the top 40 dB of the responses.

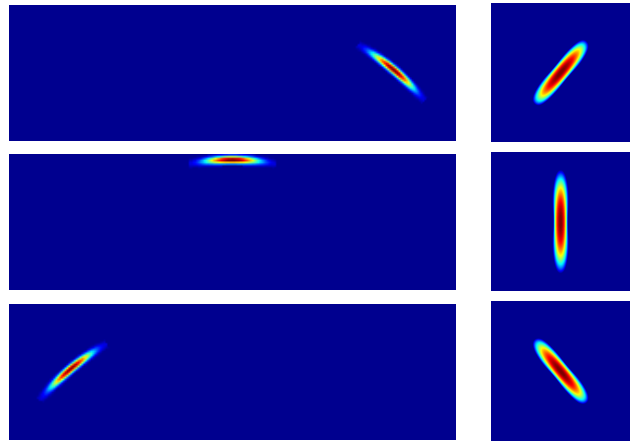


Figure 2: Windowed phase history data (left) and magnitude images (right) for reflectors with persistence angle of 20 degrees and varying peak response center azimuth angle (-40, 0, 40 degrees). The frequency support region is 5.4×18.0 GHz, and the images are 2×2 meters. The images are in logarithmic scale and show the top 40 dB of the responses.

[5, 6]. A GLRT approach has previously been used, for example, in UHF imaging of dihedrals [7, 8]. For a generic aspect response [9], we define

$$r(\phi; \phi_c, \Delta) = \begin{cases} r_0\left(\frac{\phi - \phi_c}{\Delta}\right), & -\Delta/2 < \phi < \Delta/2 \\ 0, & \text{else} \end{cases} \quad (2)$$

where ϕ_c is the azimuth of peak response and Δ describes the (frequency-dependent) beam-width of the reflector. Then, the GLRT maximizes over the unknowns ϕ_c and Δ

$$M(x, y) = \max_{\phi_c, \Delta} |I(x, y; \phi_c, \Delta)| \quad (3)$$

where M is the output magnitude image, and $I(x, y; \phi_c, \Delta)$ is a complex-valued image formed using an aperture of width Δ centered at angle ϕ_c . The response shape $r_0(\phi)$ may be incorporated into the design of a tapered window for sidelobe reduction.

Here, we consider a low-complexity approximate GLRT in which we fix $\Delta = 20$ degrees based on preliminary inspection of wide-angle X-band images of ground targets. In addition, we limit ϕ_c to a discrete set of values. Thus the approximate GLRT is formed by a maximum over several coherent subapertures, and hence non-coherently combines scattering from different subapertures. In Figure 3, we illustrate the GLRT processing for a 110 degree aperture and 500 MHz bandwidth. The top image depicts a standard tomographic image using 500 MHz bandwidth and a 110 degree aperture; the middle image shows the GLRT image using overlapped 20 degree apertures.

4. STABLE PHASE RESPONSES

With sufficiently fine resolution cells, many individual reflectors become isolated. Without scintillation of unresolved reflectors, pixel amplitudes and phases are stable with respect to small changes in viewing angle.

4.1. Resolution Enhancement

A first consequence of this stability is an ability to extrapolate bandwidth. Data adaptive filter bank methods are one class of extrapolation techniques and use estimated covariance; phase history covariance techniques include Capon and APES, while image covariance techniques include adaptive side-lobe reduction (ASR) and spatially-varying apodization (SVA) [10]. Here, we consider sparse solutions found via by convex programming. Specifically, the data collection may be modeled as a linear equation $Ax = b + n$, where n represents noise and modelling error. Determination of the sparsest reflectivity map, x , satisfying $\|Ax - b\|_2^2 < \epsilon$ is NP-hard; however, the ℓ_1 minimization

$$\min \|x\|_1 \text{ subject to } \|Ax - b\|_2^2 < \epsilon \quad (4)$$

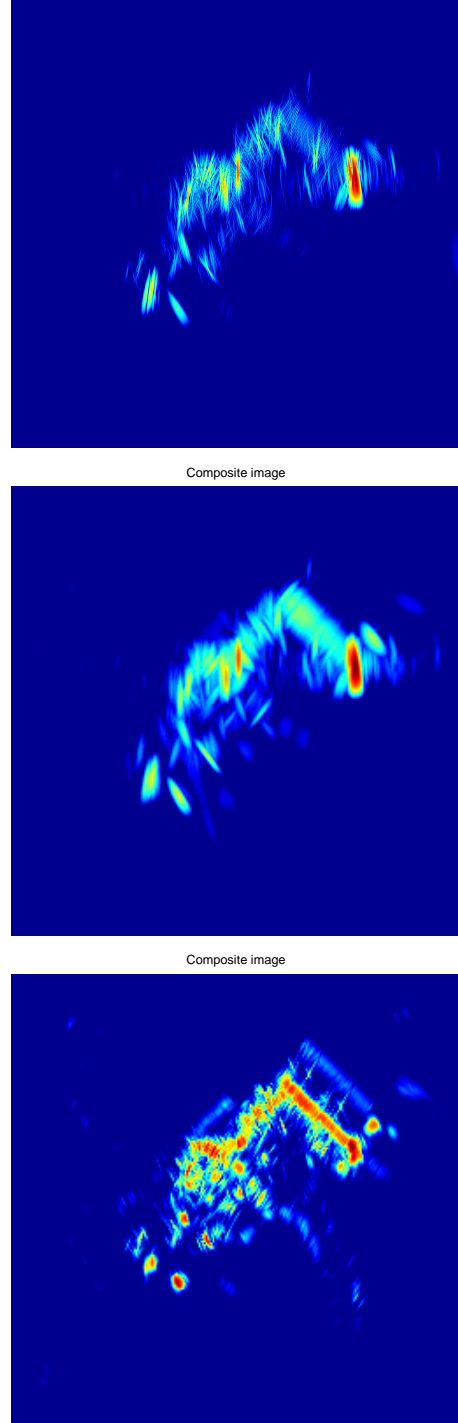


Figure 3: SAR image of the backhoe using a 110° linear aperture centered at 45° azimuth and 30° elevation with 500 MHz bandwidth and 10 GHz center frequency. (top) full aperture image; (middle) GLRT image using 20 degree subapertures; (bottom) resolution-enhanced GLRT image using ℓ_1 norm.

is a convex optimization task, and hence has unique global minimum. Further, the ℓ_1 solution is guaranteed to be close to the sparsest solution [11]. Several imaging procedures are variants of this approach [12, 13, 14]. An extrapolated phase history need not be explicitly computed in this procedure.

In Figure 3(c), we show the result of a 2D image formed using ℓ_1 -norm minimization [5]. The ℓ_1 sparse solution is used to produce a resolution-enhanced image at each 20 sub-aperture; subapertures are then combined using the GLRT processing of Section 3. Alternatively, the aspect angle of peak response may be color-coded for display.

4.2. Polarization

Resolved reflectors yield stable phase responses; a second consequence of this stability is the ability to interpret local geometry from the polarimetric response of a single pixel. The polarimetric response serves to cluster geometrically related reflectors on a target.

If full-polarization measurements are available, the amplitude is characterized by a 2×2 complex-valued matrix of scattering amplitudes. We form a Pauli-basis decomposition of this scattering matrix [15]

$$[S] = A \left\{ \cos \alpha [S]^t + e^{j\phi} \sin \alpha (\cos \theta [S]_0^d + \sin \theta [S]_{45}^d) \right\} \quad (5)$$

where $0^\circ \leq \alpha \leq 90^\circ$, $-45^\circ \leq \theta \leq 45^\circ$, and where the Surface-Dihedral-Tilted Dihedral basis is

$$[S]^t = \frac{1}{\sqrt{2}} \begin{bmatrix} 1 & 0 \\ 0 & 1 \end{bmatrix} \quad [S]_0^d = \frac{1}{\sqrt{2}} \begin{bmatrix} 1 & 0 \\ 0 & -1 \end{bmatrix} \quad (6)$$

$$[S]_{45}^d = \frac{1}{\sqrt{2}} \begin{bmatrix} 0 & 1 \\ 1 & 0 \end{bmatrix} \quad (7)$$

The matrix $[S]^t$ represents an ideal trihedral (or other odd-bounce scattering object, such as a flat plate or a sphere), $[S]_0^d$ represents a horizontally-oriented dihedral (an even-bounce scattering term), and $[S]_{45}^d$ represents a diagonally-oriented dihedral (also even-bounce). Thus, the decomposition in Equation (5) expresses the scattering matrix as a decomposition of these three canonical terms.

The three real parameters A , α and θ , in particular, provide information about the physical characteristics of the dominant scattering mechanism in the resolution cell. The parameter α represents the mixture fraction of the trihedral and dihedral components; for $\alpha = 0$ the scattering center is entirely a trihedral component, and for $\alpha = 90^\circ$ it is entirely a dihedral. The angle θ gives the orientation angle of the dihedral term. A represents the overall RCS of the scattering center. Imaging examples with color-coded polarization responses are given in the conference presentation.

4.3. Interferometric SAR

A third consequence of stable phase response is that interferometric processing may be used to estimate heights of individual reflectors, without a need for spatial averaging to achieve phase stability. Thus, a sparse 3D aperture holds potential for 3D reconstruction.

The data collection and processing are as follows. A parallel pair of apertures is synthesized at closely spaced elevation angles ψ and $\psi + \Delta\psi$; subapertures are selected such that the frequency and azimuth extent of a subaperture pair are sufficiently large to obtain high-resolution images in which many reflectors are resolved. Standard tomographic image formation is used on each subaperture to produce a pair of high-resolution images used in IFSAR processing [1]. Radar cross section is computed as the sum over available polarizations of squared pixel amplitudes, and a threshold is applied to determine significant reflectors. For each pixel exceeding the RCS threshold, we take the pixel's slant-plane downrange and crossrange location (x_s, y_s) as the reflector position in the slant plane, and compute a height from the slant plane using the difference in phase between the corresponding pixel values from the image pair; that is,

$$z_s = \frac{\lambda}{4\pi\Delta\psi} [\angle s_2 - \angle s_1] \quad (8)$$

where λ is the radar wavelength at the center frequency, $\Delta\psi$ is the elevation angle difference of the IFSAR pair, and s_1 and s_2 are the pixel values from the two images. This 3D location is transformed from the local slant-plane coordinate system to a coordinate (x, y, z) in an absolute, target-centered coordinate system. We refer to this (x, y, z) -point as an "IFSAR point."

Points are tested to remove height estimates that are likely corrupted by scintillation of unresolved reflectors. To this end, we test whether $|s_1| \approx |s_2|$ and reject points whose relative amplitudes are dissimilar; derivation and analysis of this hypothesis test is given in [16].

We associate with each IFSAR point several features: the center viewing angle $(\phi_k, \psi_k + \Delta\psi/2)$ of the subaperture IFSAR image pair, and the (possibly polarimetric) complex response. Finally, the 3D points from many subapertures may be non-coherently combined and rendered for visualization.

In Figure 4, we illustrate the set of 3D points obtained by processing the full hemisphere of viewing angles: $2 \text{ in } \times 2 \text{ in}$ resolution X-band subapertures are overlapped with centers spaced every 5 degrees in azimuth and elevation; $\Delta\psi$ is 0.05 is degrees.

5. 3D VISUALIZATION

For each two-antenna subaperture, the IFSAR and polarimetric processing procedures outlined above generate 3D

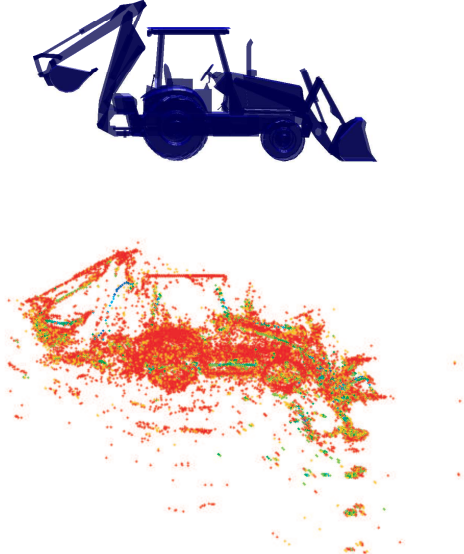


Figure 4: CAD model of backhoe (top) and 3D reconstruction of IFSAR points (bottom).

locations of reflectors that have significant RCS and are persistent in the subaperture. In addition, the processing yields a list of descriptors, or attributes [17, 18], for each point. The attributes include the center azimuth and elevation angles of the subaperture, the scattering RCS A , and the scattering matrix, as summarized, for example, by the polarimetric features α and θ . We seek to visually render these attributed points to allow near-literal interpretation of the remote scene.

The subaperture IFSAR processing allows us to non-coherently combine attributed points from many different subapertures, perhaps coming from different platforms with different bandwidths or center frequencies. Points are simply translated from slant-plane to target-centered coordinates. Significantly, the non-coherent processing allows enhanced target imaging from a diversity of viewing angles without requiring phase coherence between subapertures or across platforms.

We suggest volume cloud rendering is better suited to visualization of attributed points than volume rendering or computationally-complex surface fitting methods. In volume cloud processing, a transfer function is applied directly to points, which are then rendered in 3D. Opacity is applied based on the RCS value. Outlier points are rendered, but tend to perceptually disappear due to size and transparency of the filtered point. Clusters of points are more readily perceived. Color is applied to express one or more attributes of points. Consider three example uses of color. First, RCS can be color encoded. Second, color can be used to reveal the subaperture viewing angle, (ϕ, ψ) from which the point was generated. Third, color may be used to encode polarization.

6. EXAMPLE: 3D SPARSE APERTURE

We illustrate the near-literal 3D rendering of a ground target using a sparse aperture. While tomographic imaging would require coherent processing of a large set of Nyquist samples in both azimuth and elevation, we consider IFSAR processing of high-resolution subapertures. IFSAR apertures are extracted from the hemisphere of synthetic signatures. The subapertures are 20 degrees in azimuth and have 4 GHz bandwidth. Each IFSAR point has as attributes RCS, polarization, and viewing angle (az, el) at the center of the subaperture.

Figures 5 and 6 show two visualizations of the IFSAR points computed from subaperture images. For visualization, RCS is used to set opacity and color for each point. In Fig. 5, apertures span 360 degrees in azimuth, and elevation sample spacing is 5 degrees. Thus, eighteen IFSAR elevations are used in generating the figure, in contrast to 280 elevation samples required for Nyquist sampling of a 20 degree-by-20 degree data cube. In Fig. 6, the three limited apertures in Table 1 are used to create a notional data collection in which a target is viewed by two UAVs and one long-range standoff platform. The close-range UAV platforms provide larger elevation angles and short data collection times for large apertures.

In the conference presentations, color and animated versions of the volume cloud renderings will be presented.

7. CONCLUSION

Bandwidth and aperture can provide resolution sufficient to resolve many reflectors on a target, yielding stable amplitude and phase. The stability permits meaningful local inference of RCS, polarization, and, with IFSAR, reflector height. The non-point-like behavior of reflectors suggests non-coherent combination of large subapertures, thereby relaxing system requirements for phase coherence across very wide apertures or across multiple platforms.

The stability of scattering from resolved reflectors and non-point-like scattering physics can be exploited to provide near-literal 3D visualization of targets using sparse apertures; specifically, we have proposed high-resolution interferometric SAR image pairs distributed over wide angles. In contrast, tomographic processing in 3D requires an extremely large and dense 3D grid of observations in frequency

Table 1: Three apertures used in Fig. 6.

Platform	Sub-apertures	Elevation (deg)	Azimuth centers (deg)
1	4	5	$(-5, 0, 5, 10)$
2	19	50	$(20, 25, \dots, 110)$
3	7	$(20, 25, \dots, 50)$	$(120, 125, \dots, 150)$

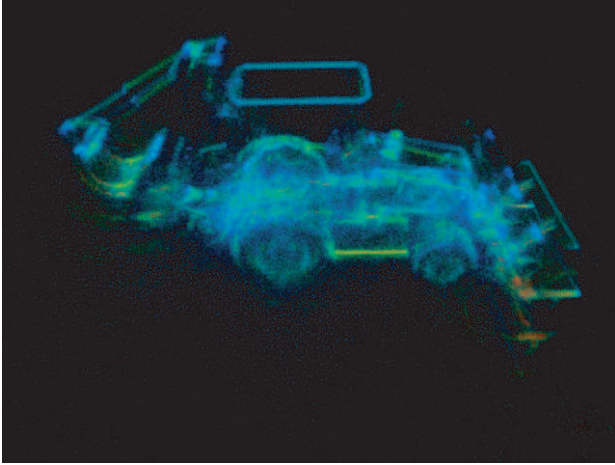


Figure 5: 3D rendering of IFSAR points from 20 degree subapertures using 18 apertures with 360-degree azimuth coverage and 5 degree elevation sampling.

and azimuth, posing significant problems in data collection and data processing. Volume cloud renderings facilitate visualization of IFSAR points and their scattering attributes.

8. REFERENCES

- [1] C.V. Jakowatz, D.E. Wahl and P.H. Eichel, *Spotlight-Mode Synthetic Aperture Radar: A Signal Processing Approach*, Kluwer Academic Publishers, Boston, MA, 1996.
- [2] D. E. Dudgeon, R. T. Lacoss, C. H. Lazott, and J. G. Verly, "Use of persistent scatterers for model-based recognition," *Proc. SPIE 2230*, pp. 356–368, Apr 1994.
- [3] L. C. Trintinalia, R. Bhalla and H. Ling, "Scattering center parameterization of wide-angle backscattered data using adaptive Gaussian representation," *IEEE Trans Antennas and Propagation*, vol. 45, pp. 1664–1668, Nov 1997.
- [4] D. Rossi and A. Willsky, "Reconstruction from projections based on detection and estimation of objects," *IEEE Trans Acoustics, Speech, and Signal Processing*, vol. 32, pp. 886–906, Aug 1984.
- [5] R. Moses, L. Potter, and M. Cetin, "Wide angle SAR imaging," *Proc. SPIE 5427*, Apr 2004.
- [6] Y. Wu and D. C. Munson, Jr., "Wide angle ISAR passive imaging using smoothed pseudo Wigner-Ville distribution," *Proc. 2001 IEEE Radar Conf.*, pp. 363–368, May 2001.
- [7] M. R. Allen and L. E. Hoff, "Wide-angle wideband SAR matched filter image formation for enhanced detection performance," *Proc. SPIE 2230*, pp. 356–368, Apr 1994.
- [8] R. D. Chaney, A. S. Willsky, and L. M. Novak, "Coherent aspect-dependent SAR image formation," *Proc. SPIE 2230*, pp. 356–368, Apr 1994.

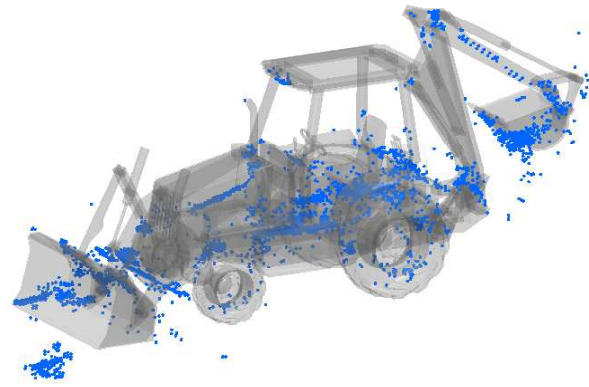


Figure 6: 3D rendering of IFSAR points from 20 degree subapertures using the three limited apertures in Table 1.

- [9] M. J. Gerry, L. C. Potter, I. J. Gupta, and A. van der Merwe, "A parametric model for synthetic aperture radar measurements," *IEEE Trans Antennas and Propagation*, vol. 47, pp. 1179–1188, July 1999.
- [10] S. DeGraaf, "SAR imaging via modern 2-D spectral estimation methods," *IEEE Trans Image Processing*, vol. 7, pp. 729–761, May 1998.
- [11] J. A. Tropp, "Just relax: Convex programming methods for identifying sparse signals in noise," submitted to *IEEE Trans Information Theory*, revised Feb 2005.
- [12] M. Cetin and W. C. Karl, "Feature enhanced synthetic aperture radar image formation based on nonquadratic regularization," *IEEE Trans Image Processing*, vol. 10, pp. 623–631, Apr 2001.
- [13] A.E. Brito, S.D. Cabrera, and C. Villalobos, "Optimal sparse representation algorithms for harmonic retrieval," *Thirty-Fifth Asilomar Conf. on Signals, Systems and Computers*, vol. 2, pp. 1407–1411, Nov 2001.
- [14] B. D. Rao and K. Kreutz-Delgado, "An affine scaling transformation for best basis selection," *IEEE Trans Signal Processing*, vol. 47, pp. 187–200, Jan 1999.
- [15] E. Ertin and L. C. Potter, "Polarimetric classification of scattering centers using M-ary Bayesian decision rules," *IEEE Trans Aerospace and Electronic Systems*, vol. 36, pp. 738–749, July 2000.
- [16] C. Austin and R. Moses, "IFSAR processing for 3D target reconstruction," *Proc. SPIE 5808*, Mar 2005.
- [17] L. C. Potter and R. L. Moses, "Attributed scattering centers for SAR ATR," *IEEE Trans Image Processing*, vol. 6, pp. 79–91, Jan 1997.
- [18] G. R. Benitz, "High-definition vector imaging," *Lincoln Lab. J.*, vol. 10, no. 2, pp. 147–170, 1997.